



**HAL**  
open science

# A study on the effects of an explosion in the Pantheon of Rome

Filippo Masi, Ioannis Stefanou, P Vannucci

► **To cite this version:**

Filippo Masi, Ioannis Stefanou, P Vannucci. A study on the effects of an explosion in the Pantheon of Rome. 2017. hal-01493006v1

**HAL Id: hal-01493006**

**<https://hal.science/hal-01493006v1>**

Preprint submitted on 20 Mar 2017 (v1), last revised 19 Dec 2017 (v2)

**HAL** is a multi-disciplinary open access archive for the deposit and dissemination of scientific research documents, whether they are published or not. The documents may come from teaching and research institutions in France or abroad, or from public or private research centers.

L'archive ouverte pluridisciplinaire **HAL**, est destinée au dépôt et à la diffusion de documents scientifiques de niveau recherche, publiés ou non, émanant des établissements d'enseignement et de recherche français ou étrangers, des laboratoires publics ou privés.

# A study on the effects of an explosion in the Pantheon of Rome

F. Masi<sup>1,2</sup>, I. Stefanou<sup>2</sup>, and P. Vannucci<sup>\*3</sup>

<sup>1</sup>Department of Industrial Engineering, University of Florence (I).

<sup>2</sup>Laboratoire Navier - UMR8205, CNRS, ENPC & IFSTTAR.  
Université Paris-Est, Marne La Vallée (F)

<sup>3</sup>LMV, Laboratoire de Mathématiques de Versailles - UMR8100 CNRS & UVSQ.  
University Paris-Saclay, Versailles (F)

March 18, 2017

---

## Abstract

This is an investigation on the effects of an explosion on the structure of the Pantheon of Rome. A numerical simulation is performed where the blast is modeled in the air domain by the JWL model and its effects on the structure by a nonlinear constitutive law based upon a damage model for no-tension materials.

**Key words:** blast effects; no-tension materials; explosions; impact engineering; Pantheon of Rome.

---

## 1 Introduction

We propose in this paper a study on the structural effects of an explosion in the Pantheon of Rome. Highly representative monuments are unfortunately too often the objective of violences and iconoclastic destructions: the examples of the Parthenon in 1687, the Cathedral of Reims in 1914, the Buddha statues of Bamyan in 2001 and the more recent destructions at Palmyra in 2015 and 2016 are just some few examples of how much symbols of a cultural heritage proper to a nation, to a civilization or to a religion, are threatened.

Research on the effects of an explosion on monumental architectures are hence interesting for assessing the potential effects of a blast onto a monument structure and also for helping in designing reinforcements or any other possible passive protection device aiming at reducing the consequences of an explosion on the structure of the monument.

This domain is still almost unexplored; in fact, the most part of papers concerning the effects of an explosion on a civil structure regard modern reinforced concrete or steel

---

\*Corresponding author: Paolo VANNUCCI. LMV, 45 Avenue des Etats-Unis. 78035 Versailles, France  
E-mail: [paolo.vannucci@uvsq.fr](mailto:paolo.vannucci@uvsq.fr)

structures with simple geometries, normally squared buildings, [Remennikov, 2003], [Ngo et al., 2007], [Kocczaz et al., 2008], [Draganic and Sigmund, 2012].

This is not the case of monumental structures that have often a complex geometry, sometimes very articulated, which renders the assessment of the blast loads strongly case dependent and affects the type of simulation. This point is tackled in Sect. 3, where a short account of the state of the art for what concerns the simulation of blast loads is given and, on its base, the choice of the method used for the case of Pantheon is justified.

On the other hand, monumental structures are either masonry-like or timber structures, or both of them at the same time. In particular, monuments constituted by masonry-like materials have a structural response strongly affected by the no-tension behavior of the material. This is a key point, considered in Sect. 4.

A particular attention must hence be paid to the procedure to be used for numerical simulations, that must account, on one hand, for the hypervelocity of the phenomenon and, on the other hand, for the peculiar constitutive law of the material, that must be able to describe the non-linear phenomenon of damage, i.e. of cracks propagating into the body of the structure as a consequence of the blast actions. Considerations about the procedure used for the numerical simulations are given in Sect. 5.

These last are presented in Sect. 6. All the results given in this paper are normalized; this does not affect, anyway, the quality of the results and in particular the way the blast load interacts with the structure of the monument and how its structure responds to such a load, which are the topics of this paper.

But let us start by briefly introducing, in Sect. 2, the object of this study, the Pantheon of Rome.

## 2 The Pantheon of Rome

The Pantheon is one of the most admired and studied monuments of ever. The building that has come to us is actually the fourth Pantheon, built upon the rests of previous temples of classical rectangular form, by the Emperor Hadrian, since A.D. 118 to about 128, or later, perhaps until 140, under Emperor Antoninus Pius.

The Pantheon is probably the joint work of Hadrian and of the Nabatean great architect Apollodorus of Damascus, at least until 121, when seemingly he was first exiled by Hadrian and then executed in 125, according to Dione Cassius. Apollodorus was the architect of many great constructions during the reign of the Emperor Trajan, namely of the great bridge over the Danube, of the Trajan's Forum and Markets, of the artificial harbour of Porto and so on.

The Pantheon has inspired number of architects during the centuries, especially during the Neo-Classical period, e.g. P. Bianchi in the church San Francesco di Paola in Naples (1816-46), F. Bonsignore in the church Gran Madre di Dio in Turin (1818-31) or T. Jefferson in The Rotunda of the University of Virginia (1822-26).



Figure 1: The Pantheon of Rome (from [Pulvirenti, 2014]).

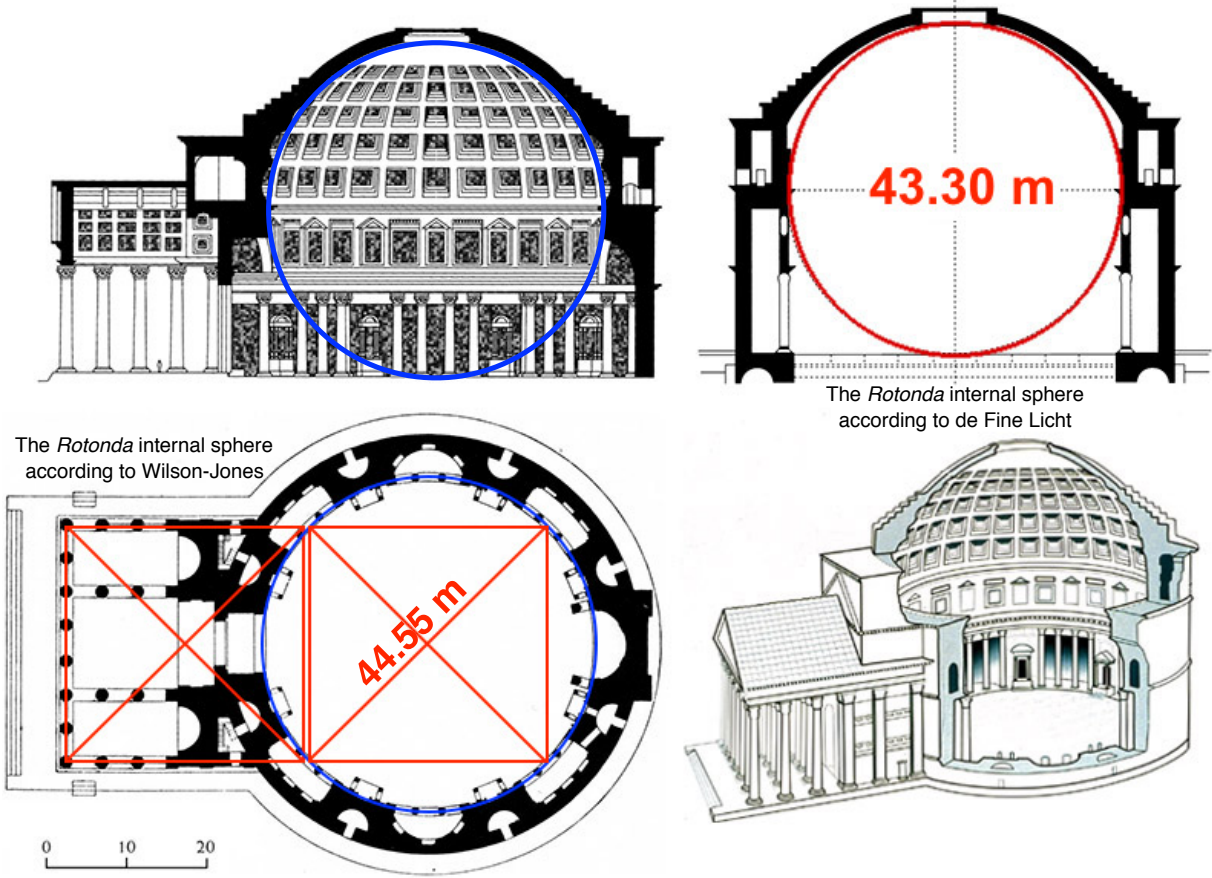


Figure 2: Scheme and dimensions of the Pantheon (from [Pulvirenti, 2014]).

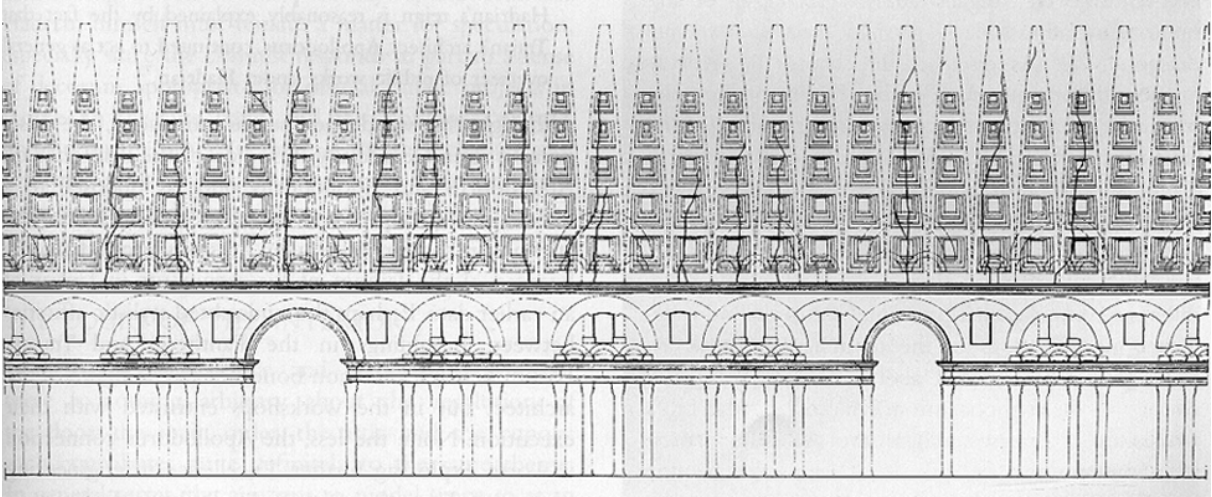


Figure 3: Meridional cracks in the *Rotonda's* dome (after [Terenzio, 1934]).

The main body of the Pantheon, the so-called *Rotonda* recalls, probably intentionally, the celebrated discovery of Archimedes of the volume of a sphere inscribed in a cylinder, [Boyer, 1968]. In fact, see Fig. 2, the *Rotonda* is composed by a cylinder whose inscribed sphere is coincident, for its upper part, with the dome, while its bottom touches the ground. The touch of Archimedes is present also with regard to another aspect: the coffering that is sculpted in the intrados of the dome is subdivided into 28 parts, and it was Archimedes that studied the related problem of partitioning a circle into 7 parts. The coffering, besides its aesthetic role, serves also to reduce the dome's weight.

The diameter of the dome is of 43.30 m, according to the measurements of de Fine Licht, [K. de Fine Licht, 1968], [Mark, 1990]. However, according to Wilson-Jones, [Wilson-Jones, 2000], [Como, 2013], the right measure of the diameter is 44.55 m and it corresponds to the circle passing through the axes of the columns in the interior of the *Rotonda*. This measure equals 150 Roman feet and is exactly identical to  $\sqrt{2}$  times the width of the *pronaos*, the entrance *portico* of the monument: in the interpretation of Wilson-Jones, the *Rotonda* perfectly circumscribes a square equal to that of the *pronaos*, see Fig. 2.

The Pantheon's dome is, still today, the largest dome in the world, apart the modern realizations in reinforced concrete. In fact, it is larger than the dome of Saint Peter in Vatican, whose diameter is of 42 m, and also of the octagonal dome of F. Brunelleschi, in Santa Maria del Fiore at Florence, whose base is circumscribed to a circle of 41.57 m. However, unlike these two famous domes, and also of other ones, made by bricks, the Pantheon's one is made of concrete, a technique already mastered by Apollodorus in other previous works (e.g. the vault of the Great Hall in the Trajan's markets in Rome, see [Perucchio and Brune, 2008], [Perucchio and Brune, 2009]).

If the intrados of the dome is sculpted by a coffering, the external lowest part of the dome is modeled by stepped rings. The function of these stepped rings, and more generally the structural behavior of the *Rotonda*, has been studied by Mark and Hutchinson, [Mark and Hutchinson, 1986], [Mark, 1990]. For their study, the first attempt to apply finite element analysis to Roman structures, they used a rather simplified bi-dimensional model of the *Rotonda*, exploiting axe-symmetric conditions. The results are rather troubling: according to Mark and Hutchinson, and contrarily to what commonly thought, the step-

rings do not contrast the hoop tension in the lowest part of the dome, because actually the dome is spread of cracks that have an almost meridional direction and that stop at  $\sim 57^\circ$  above the equatorial plane passing through the dome's base. In this zone, the hoop stress begins to be compressive.

The distribution of these cracks, Fig. 3, was detailed in 1934 by A. Terenzio, the Superintendent of the Monuments of Latium, who had carried on a series of inspections on the dome of the *Rotonda* after that some fragments had fallen down, [Terenzio, 1934].

We cannot establish here what is the true origin of these cracks, but certainly they are to be modeled to have a correct response of the structure to both gravity and blast. In fact, on one hand, the cracks undoubtedly change the stress regime of the *Rotonda*, on the other hand, they considerably affect the response of the structure to a blast by a special local mechanism, as we will see in Sect. 6.2.

### 3 Modeling the blast actions

An explosion is an extremely rapid and exothermal chemical reaction that lasts just few milliseconds. During detonation, hot gases, produced by this chemical reaction, expand quickly and, for the hot temperatures produced instantaneously, the air around the blast expands too. The result is a blast shock wave, characterized by a thin zone of air propagating spherically much faster than the sound speed, through which pressure is discontinuous. We give here just a brief account of a blast phenomenon, more details can be found in [Vannucci et al., 2017a].

To better understand all the mechanics of a blast, let us first introduce some quantities, used in the following:

- $W$ : explosive mass;
- $R = ||q - o||$ : distance of a point  $q$  from the detonation point  $o$ ;
- $P_o$ : ambient pressure;
- $P_s$ : overpressure due to the blast; it is the pressure in the air relative to  $P_o$ ;
- $P_r$ : reflected overpressure: the pressure, relative to  $P_o$ , acting at a point  $q$  of a solid surface when hit orthogonally by a shock-wave;
- $t_A$ : arrival time, i.e. the instant at which the shock-wave peak arrives at  $q$ ;
- $t_o$ : positive phase duration;
- $t_{o-}$ : negative phase duration;

Fig. 4 represents an ideal profile of the overpressure  $P_s(q, t)$  produced by a blast. When the shock wave arrives at  $q$ , after  $t_A$  from detonation, the pressure instantaneously increases, from the ambient pressure  $P_o$  to a peak for  $P_s$ , which is a strong discontinuity.

For  $t > t_A$  the overpressure decreases extremely fast, with an exponential rate, until time  $t_A + t_o$ , when  $P_s = P_o$ , which marks the end of the so-called positive phase. After  $t_A + t_o$  we have the negative phase: the pressure decreases with respect to  $P_o$  and then it returns to

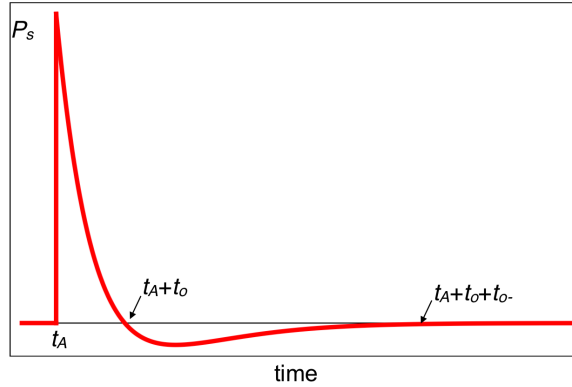


Figure 4: Scheme of the time variation of the pressure due to a blast.

$P_o$  after a time  $t_{o-} > t_o$ . Anyway, during the negative phase the decrease of the pressure is much lower, in absolute value, than the peak pressure of the positive phase, so usually the negative phase can be neglected for structural analyses, though it can be important in some particular cases, due to its duration, always much longer than the positive phase. Such a behavior is idealized: different perturbations of the curve in Fig. 4 can occur, due to various causes.

The shock wave is the main mechanical effect of a blast on a structure, but not the only one: the hot gases, expanding, produce the so-called dynamic pressure, least in value with respect to the shock wave and propagating at a lesser speed, while the impinging shock wave can be reflected by solid surfaces and act again on other surfaces as reflected shock waves.

The overpressure  $P_s$  at a point  $q$  decreases with both the time  $t$  and the distance  $R$ . Generally, the time rate decrease is much greater than the space rate decrease: the blast overpressure is really like a very localized pressure wave that propagates at high speed and whose intensity decreases, like for any other wave, with the travelled distance.

$P_r$  is the pressure that acts on a surface impinged by the incident overpressure  $P_s$ . The peak of  $P_r$  is normally much greater than that of  $P_s$  measured at the same point in the absence of any surface.

In the case of explosions on monuments, we are concerned with surface blasts, i.e. with detonation points close to the ground surface, which give hemispherical overpressure waves. The closeness of the blast to the ground results in an augmentation of the shock overpressure, because the ground reflects and amplifies the overpressure wave.

The simulation of a blast can be conducted using different approaches, the most widely used being three: the JWL model, the CONWEP model and the TM5-1300 model. They are briefly described in the following.

JWL stands for Jones, Wilkins and Lee, the authors of this model, [Jones and Miller, 1948], [Wilkins, 1964], [Lee et al., 1968]. The JWL model is physically based: the laws of thermodynamics are used to recover the physics of a chemical blast. It allows a complete description of a blast phenomenon, including the propagation of the shock-wave in a medium, e.g. air, its reflection on solid surfaces and the expansion of the hot gases, i.e. the dynamic pressure.

The JWL model gives the overpressure  $P_s$  as function of different parameters:

$$P_s = A \left( 1 - \frac{\omega \rho}{R_1 \rho_0} \right) \exp \left( -R_1 \frac{\rho_0}{\rho} \right) + B \left( 1 - \frac{\omega \rho}{R_2 \rho_0} \right) \exp \left( -R_2 \frac{\rho_0}{\rho} \right) + \omega \rho E_m. \quad (1)$$

$A$ ,  $B$ ,  $R_1$ ,  $R_2$  and  $\omega$  are parameters depending upon the explosive type, along with  $\rho_0$ , its density, while  $\rho$  is the density of the detonation products and  $E_m$  is the internal energy per unit mass. The detonation velocity  $v_D$  and the Chapman-Jouguet pressure  $p_{cj}$  need to be specified too.

The use of JWL model allows a rather precise and complete simulation of the blast phenomenon, but its drawback is the need of discretizing, finely, the charge and the fluid domain, that can be very large, besides the structure if a coupled structural analysis is to be done. Such multi-physics transient problems, with a strong coupling between fluid and structure dynamics, lead to numerical simulations that can be, in the case of a monument, very heavy.

Because less heavy, computationally speaking, empirical methods are more often used in the calculations. With such models, based upon the results of experimental tests, the characteristic parameters of the explosive serve to calculate the overpressure shock-wave and its propagation speed. The wave propagates spherically from the detonation point  $o$  to the elements of the structure. The distance of  $o$  from any impact point  $q$  on a surface of the structure and the inclination of the perpendicular to the surface with respect to the vector  $q - o$  are the only geometric parameters needed by the models.

In fact, these models make abstraction from the fluid medium and consider just the incident wave, not the reflected ones, nor the dynamic pressure, that can be anyway calculated afterward.

The two most commonly used empirical models are based upon different but related studies of the U.S. Army Corps of Engineers (USACE): the document [USACE, 1986], containing the model CONWEP, and the Technical Manual TM5-1300, [USACE, 1990], completed by successive documents, [USACE, 2008]. The Joint Research Center of the European Union has produced in 2013 a Technical Report, [Karlos and Solomos, 2013], substantially referring to these two last documents and to another Technical Report of the U.S. Army, [Kingery and Bulmash, 1984].

The empirical models cannot describe as finely as the JWL model all the effects of a blast, especially because they neglect reflected waves. The effect of these last can be very important, especially for internal blasts: depending upon geometry, the concentration of the reflected waves can give rise to local effects that can be greater than the original shock wave. In the case of a blast inside monumental-like structures, these phenomena can assume a great importance. Authors have shown, for instance, that in the case of a vaulted structure, a localized shock wave produced by the reflected waves can hit the vault with an overpressure far greater than that produced directly by the original impinging shock wave, [Vannucci et al., 2017a].

The case of the *Rotonda* is hence particularly interesting: by its geometry, focalizing effects can happen and be determinant. That is why we have chosen to study the problem of a blast inside the Pantheon using the JWL model, that allows for modeling completely the explosion. This needs the discretization not only of the structure, to perform the coupled

structural analysis, but also of the air volume inside and partly outside the Pantheon. This is a step forward with respect to a previous study of the authors, where the CONWEP model was used, [Vannucci et al., 2017b]. Finally, we have a very huge numerical model, needing a considerable computational effort; this aspect is detailed in Sect. 5.

## 4 Modeling the material behavior

The Pantheon is made by different materials: bricks, mortar and concrete, for the cylindrical part of the *Rotonda*, granite for the columns inside and concrete for the dome. The cylindrical part is actually composed also by pillars and arches, having a structural role and merged in the wall, whose thickness is of about 6 m. Concerning the dome, it is more correct to say that it is composed of *concretes*, because the Romans used different types of concrete, from the heaviest one in the lower part, whose thickness is  $\sim 5.9$  m, to the lightest one in the upper part of the dome, where the thickness decreases to  $\sim 1.5$  m, see Fig. 5.

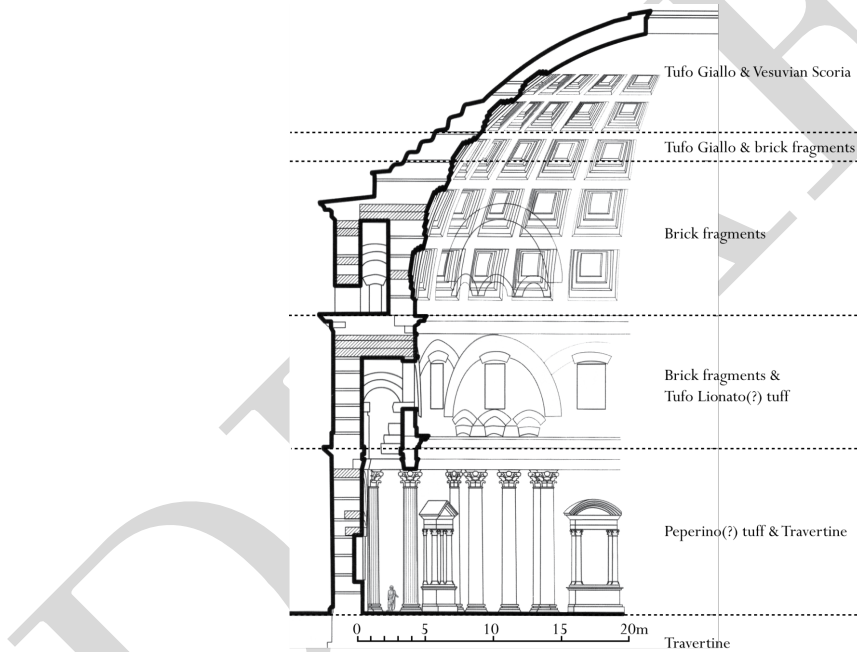


Figure 5: Materials composing the *Rotonda* (after [Lancaster, 2005])

### 4.1 The mechanical model of the materials

Masonry and concrete share a peculiarity: they have a low strength to tensile stresses, so small that often they are modeled as no-tension materials. In this study, we have used the same mechanical model for the constitutive law of the concretes composing the dome or the foundations, the masonry of the cylindrical part and the granite of the columns. We precise that we have modeled the masonry as an isotropic homogeneous material, as it is almost impossible, for such a large structure, to model precisely the actual disposition

of the bricks composing the pillars and numerous arches included in the masonry of the *Rotonda*, see Fig. 5.

The constitutive law that we have used considers a linear elastic behavior in compression, with an unlimited strength. This corresponds to the normal compression response of masonries and concretes and to the fact that normally in monumental structures compression remains far below the compressive strength of the material, cf. [Heyman, 1995], [Stefanou et al., 2015].

In tension, the material is assumed to be linearly elastic until the maximum principal stress does not exceed the tensile strength. Actually, a small, but not null, tensile strength  $f_t$  is considered for the material. When  $f_t$  is exceeded, a damage of the material occurs. This is modeled using the nonlinear brittle cracking model proposed in [Hillerborg et al., 1976]. In this model, a crack appears when the maximum principal stress over an element exceeds its tensile strength  $f_t$ . The crack forms in the plane orthogonal to the direction of the principal stress exceeding the tensile limit, see also [ABAQUS, 2016].

An energy criterion, using the fracture energy  $G_f$ , is used to model the cracks propagation. This allows to minimize mesh dependency due to the softening behavior of the material and to dissipate adequately the energy. We have used a simplified Hillerborg's law, shown in Fig. 6, to represent the tensile part of the constitutive law: in tension, the elastic phase is followed by a piecewise linear softening one, modeling the damage of the material.

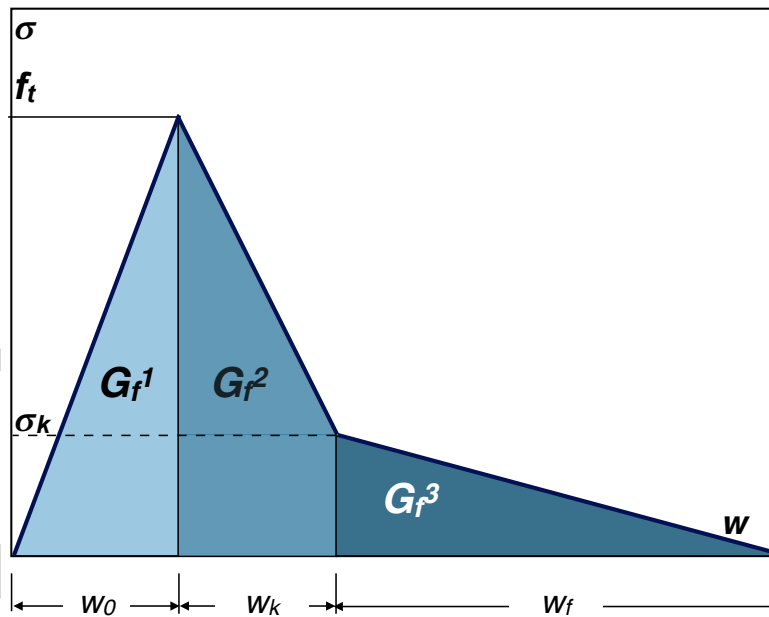


Figure 6: Simplified Hillerborg's model used as constitutive law in tension.

Referring to Fig. 6, the fracture energy for normal tensile stresses is defined as

$$G_f = G_f^1 + G_f^2 + G_f^3 = \int_0^{w_0} \sigma dw + \int_{w_0}^{w_k} \sigma dw + \int_{w_k}^{w_f} \sigma dw, \quad (2)$$

where  $\sigma$  is the maximum principal stress;  $w$  is the displacement normal to the crack surface, defined as the product of the normal strain  $\varepsilon$  and a characteristic length  $h$ , i.e.

$w = \varepsilon h$ ;  $w_0$  is the normal displacement corresponding to  $f_t$ ,  $w_k$  that relative to the kink point, with stress  $\sigma_k$ , and  $w_f$  the one corresponding to the complete loss of strength.

Because the assumed constitutive law is piecewise linear, putting, like in [Brune, 2010],

$$\Psi = \frac{\sigma_k}{f_t}, \quad \zeta = \frac{w_k}{w_f}, \quad (3)$$

the three integrals in eq. (2) become ( $E$  is the Young's modulus)

$$\begin{aligned} G_f^1 &= \int_0^{w_0} \sigma dw = \frac{f_t w_0}{2} = \frac{f_t^2}{2E} h, \\ G_f^2 &= \int_{w_0}^{w_k} \sigma dw = \frac{f_t}{2} (1 + \Psi) (\zeta w_f - \frac{f_t}{E} h), \\ G_f^3 &= \int_{w_k}^{w_f} \sigma dw = \frac{f_t}{2} \Psi (1 - \zeta) w_f, \end{aligned} \quad (4)$$

so that

$$G_f = \frac{f_t}{2} \left[ (\Psi + \zeta) w_f - \Psi h \frac{f_t}{E} \right]. \quad (5)$$

Normally,  $G_f$ ,  $E$  and  $f_t$  are known for a given material; fixing  $\Psi$  and  $\zeta$  allows to find the value of  $w_f$  :

$$w_f = \frac{1}{\Psi + \zeta} \left( \frac{2G_f}{f_t} + \Psi h \frac{f_t}{E} \right). \quad (6)$$

The question is now how to fix the material characteristics; this point is addressed in the next Section.

## 4.2 The choice of the material characteristics

Different material characteristics must be fixed for each material: the density  $\rho$ , the Young's modulus  $E$ , the Poisson's ratio  $\nu$ , the fracture energy  $G_f$ , the tensile strength  $f_t$  and the two ratios  $\Psi$  and  $\zeta$ .

We have considered five zones for the materials of the *Rotonda*, corresponding to those indicated in Fig. 5: foundations, brick-faced concrete of the cylindrical wall, lower, intermediate and upper zone of the dome. In addition, we have considered apart the material of the columns in the interior of the *Rotonda*, made of granite. The materials data are shown in Tab. 1 and their location in the *Rotonda* is shown in Fig. 7, while their choice is discussed below.

The concrete densities have been fixed upon the indications given in [Mark and Hutchinson, 1986]. About the other quantities, the choice is much more problematic. Though we know today rather well the behavior of light concretes, according to historians and researchers in mechanics of ancient monuments, the physical properties of concretes and mortars of the past have quite different characteristics. Moreover, the data that can be found in the literature about ancient concretes are often quite different and most of all fragmentary. The only reliable data about the Pantheon were the densities. So we needed

Table 1: Materials data

Material	Part	$\rho$ [kg/m <sup>3</sup> ]	$E$ [GPa]	$G_f$ [J/m <sup>2</sup> ]	$f_t$ [MPa]	$\nu$	$\Psi$	$\zeta$
Granite	Columns	2500	55.3	17.5	3.50	0.16	0.25	0.50
Concrete 1	Foundations	2000	13.5	62.1	0.68	0.20	0.35	0.15
Concrete 2	Cylindrical wall	1750	7.0	59.4	0.63	0.20	0.35	0.15
Concrete 3	Lower dome	1600	4.6	57.7	0.60	0.20	0.35	0.15
Concrete 4	Intermediate dome	1500	3.6	56.6	0.58	0.20	0.35	0.15
Concrete 5	Upper dome	1350	3.0	55.0	0.55	0.20	0.35	0.15

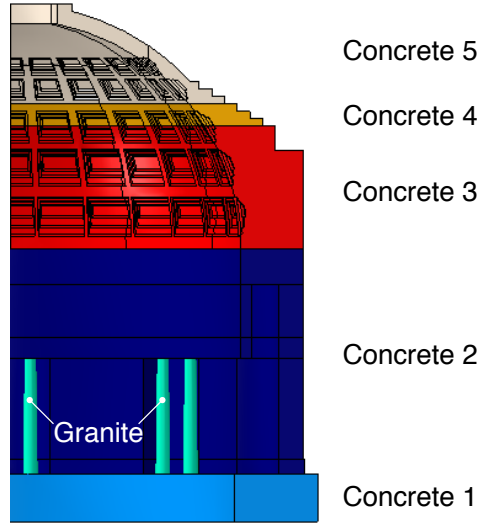


Figure 7: Location of the materials in Tab. 1.

a rationale linking in some way the other material parameters to densities in such a way that, starting from few known data, the other ones could be determined.

First of all, for all the concretes, we have put  $\nu = 0.2$ , a mean value often used for the concrete Poisson's coefficient in ancient monuments, see e.g. [Perucchio and Brune, 2009].

About the Young's modulus  $E$ , the question was more delicate. Tests done on Roman mortars and concretes give very low values for  $E$ , see [Brune, 2010], [Jackson et al., 2009], [Jackson et al., 2014]. In his PhD thesis, Brune gives a table reporting, as a function of the curing duration, some typical values of different material parameters, in particular  $E$ ,  $f_t$ ,  $G_f$ ,  $\Psi$  and  $\zeta$ . Such values are reported in Tab. 2.

Of course, the interesting values for the present analysis are those referring to a set of 180 days. Also comparing the value of  $E$  given by Brune with other tests, see e.g. [Jackson et al., 2009], [Jackson et al., 2014], [Brune et al., 2010], [Samuelli-Ferretti, 1996], it is likely to consider the value  $E = 3.37$  GPa as a, more or less, minimum for the Young's modulus (this value is referred to a concrete whose density is 1540 kg/m<sup>3</sup>).

Another value that can be extrapolated from the literature, is that concerning  $E$  for the cylindrical wall; it is composed by concrete and masonry and we have found a reliable

Table 2: Roman concrete properties as function of the set (after [Brune, 2010]).

Set [Days]	$E$ [GPa]	$f_t$ [MPa]	$G_f$ [J/m <sup>2</sup> ]	$\Psi$	$\zeta$
28	1.00	0.08	5	0.50	0.10
90	2.90	0.47	45	0.40	0.10
180	3.37	0.55	55	0.35	0.15

value for ancient masonry in [Como, 2013]:  $E = 6.6$  GPa. So, rounding the above values, we have put  $E = 3$  GPa for concrete 5, the lightest one and  $E = 7$  GPa for concrete 2. The other values can be determined upon a rule stating the dependence of  $E$  on  $\rho$ . We did not find it in the literature about ancient concretes and the scarcity of data about these materials did not allow us to extrapolate such a rule.

That is why we have considered modern technical recommendations about lightweight concretes, [ACI, 1999], [FIB, 2000]. The following law is proposed in [Sanpaolesi and Formichi, 2009] about the Young's modulus:

$$E = 22 \left( \frac{f_c}{10} \right)^{0.3} \left( \frac{\rho}{2200} \right)^2, \quad (7)$$

with  $E$  in GPa,  $\rho$  in kg/m<sup>3</sup> and  $f_c$ , the mean compressive strength, in MPa. So, what is apparent from this relation is that  $E$  is a quadratic function of  $\rho$ . We have hence looked for a law representing  $E$  satisfying this rule, giving a minimum of  $E$  for  $\rho = 1350$  kg/m<sup>3</sup> and the two values given above for concrete 5 and concrete 2. Some simple passages give the relation

$$E = 2.5 \times 10^{-5} \rho^2 - 0.0675 \rho + 48.5625, \quad (8)$$

with  $E$  in GPa and  $\rho$  in kg/m<sup>3</sup>. This allows to have an estimation of  $E$  also for the other concretes.

About the tension strength  $f_t$ , the only reliable datum is that of Brune, see Tab. 2:  $f_t = 0.55$  MPa. We attribute this value to concrete 5, the lightest one. Like for  $E$ , we need hence to put in relation  $f_t$  with  $\rho$ . We still use a relationship proposed for modern lightweight concrete, [Sanpaolesi and Formichi, 2009]:

$$f_t = 0.3 f_{ck}^{2/3} \left( 0.4 + 0.6 \frac{\rho}{2200} \right), \quad (9)$$

where  $f_{ck}$  is the characteristic value of the statistical distribution of  $f_c$ . It is likely that the compressive strength of the concretes in Tab. 1 do not change considerably. Then, making the assumption that  $f_{ck}$  is practically constant, we get the following relation between the values of  $f_t$  for two different concretes:

$$\frac{f_{t1}}{f_{t2}} = \frac{0.4 + 0.6 \frac{\rho_1}{2200}}{0.4 + 0.6 \frac{\rho_2}{2200}}. \quad (10)$$

So, putting  $f_{t1} = 0.55$  MPa and  $\rho_1 = 1350$  kg/m<sup>3</sup>, we get the following linear relation for  $f_t$  as function of  $\rho$ :

$$f_t = 3.25 \times 10^{-4} (880 + 0.6 \rho), \quad (11)$$

with  $f_t$  in MPa and  $\rho$  in  $\text{kg/m}^3$ . This relation allows us to have an estimation of  $f_t$  also for the other concretes of the *Rotonda*.

Concerning the fracture energy  $G_f$ , once more we have attributed the value of  $55 \text{ J/m}^2$  of Tab. 2 to concrete 5. The data concerning  $G_f$  in the literature are even more questionable than those of the other material parameters: they are considerably affected by the experimental or numerical procedure used for its evaluation besides the intrinsic properties of the material, like the size of the aggregates, the curing process and so on. As a consequence, the spread of data is considerable, see for instance [Hillerborg, 1985], [Weerheijm and Vegt, 2010]. Hence, once more we have looked for a relation between  $G_f$  and another known material parameter of concrete.

In [Dehn, 2004] the author gives a linear relation between  $G_f$  and the tensile strength  $f_t$  for lightweight concretes with natural sand, which is the case of the concretes of the *Rotonda*:

$$G_f = 24 + 16f_t, \quad (12)$$

with  $G_f$  in  $\text{J/m}^2$  and  $f_t$  in MPa. So, for two different concretes, we get

$$\frac{G_{f1} - 24}{G_{f2} - 24} = \frac{f_{t1}}{f_{t2}}, \quad (13)$$

and putting, as indicated above,  $G_{f1} = 55 \text{ J/m}^2$  and  $f_{t1} = 0.55 \text{ MPa}$ , data relative to concrete 5 in Tab. 1, we get the linear relation

$$G_f = 24 + 56.36f_t, \quad (14)$$

allowing us to obtain an estimation of  $G_f$  for all the other concretes. The values of  $E$ ,  $f_t$  and  $G_f$  so obtained for all the concretes are indicated in Tab. 1.

For what concerns the ratios  $\Psi$  and  $\zeta$  we have put  $\Psi = 0.35$  and  $\zeta = 0.15$ , as suggested by Brune, see Tab. 2.

For the granite of the columns, we have taken the values found in [Buyukozturk, 1993] and we have put  $\Psi = 0.25$  and  $\zeta = 0.50$ .

Using eqs. (3) and (6), along with the Hooke's law for the value of  $w_0$ ,

$$w_0 = \frac{f_t}{E}h, \quad (15)$$

we get also all the other parameters defining the constitutive law represented in Fig. 6. These parameters are shown in Tab. 3. The values of  $w_0$ ,  $w_k$  and  $w_f$  have been calculated for a reference length  $h = 100 \text{ mm}$ .

In Fig. 8 we show the diagrams of the constitutive law  $\sigma - w$ . The diagram of the granite has been reduced by a factor 4, for graphical reasons.

It is worth noting that the values of the different material parameters are close to experimental data measured on ancient Roman concretes, see [Lamprecht, 1984], [Jackson et al., 2009], [Brune, 2010], [Brune et al., 2010] and [Jackson et al., 2014]. They represent hence a plausible variation of such parameters with the concrete density.

The properties of Roman concrete are remarkable when compared to modern concretes: the low value of the Young's modulus, the high tensile strength and the important fracture

Table 3: Materials parameters defining the constitutive law

Material	$E$ [GPa]	$G_f$ [J/m <sup>2</sup> ]	$f_t$ [MPa]	$\Psi$	$\zeta$	$\sigma_k$ [MPa]	$w_0$ [mm]	$w_k$ [mm]	$w_f$ [mm]
Granite	55.3	17.5	3.50	0.25	0.50	0.88	0.006	0.008	0.015
Concrete 1	13.5	62.1	0.68	0.35	0.15	0.24	0.005	0.006	0.371
Concrete 2	7.0	59.4	0.63	0.35	0.15	0.22	0.009	0.058	0.385
Concrete 3	4.6	57.7	0.60	0.35	0.15	0.21	0.013	0.059	0.395
Concrete 4	3.6	56.6	0.58	0.35	0.15	0.20	0.016	0.060	0.403
Concrete 5	3.0	55.0	0.55	0.35	0.15	0.19	0.018	0.062	0.413

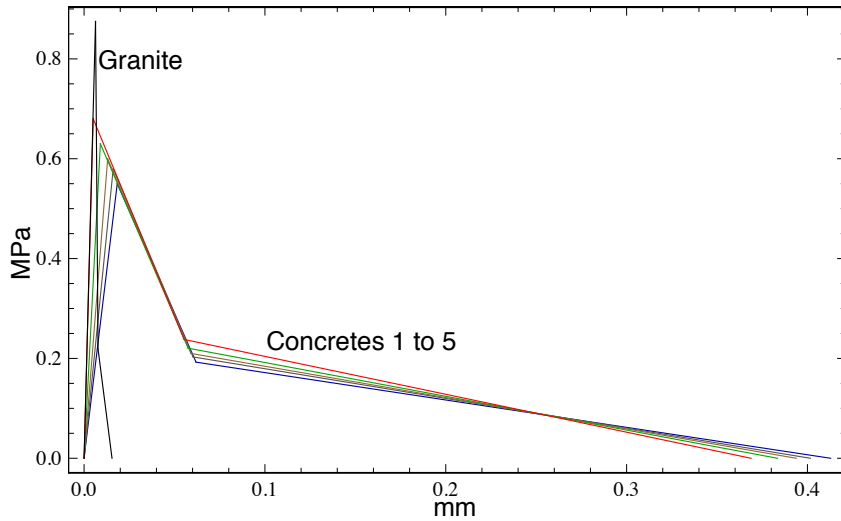


Figure 8: Tensile constitutive law of the materials (for  $h = 100$  mm).

energy confer to Roman concretes good properties of ductility and toughness, that render such materials particularly suited for energy dissipation.

## 5 The numerical procedure

The use of the model JWL for the blast simulation needs, as already mentioned, a meshing not only of the Pantheon's structure, but also of the air volume interested by the explosion, in this case the internal volume of the *Rotonda* and also a volume around the two openings, the entrance door and the *oculus*, the "Pantheon's eye", the round opening at the dome's top, with a neat diameter of  $\sim 7$  m, [K. de Fine Licht, 1968]. The details on the models of the air volume and of the structure and the procedure used for their numerical validation are given below, separately for the two parts. Using the symmetry of the structure, see below Fig. 13, we have modeled just one half of the structure and of the air domain. This allows, for the same computing effort, to obtain a more detailed model, i.e. a finer discretization. All the computations have been done with the code ABAQUS, [ABAQUS, 2016].

## 5.1 Validation of the fluid domain finite volumes model

The model of the air domain is shown in Fig. 9. The air domain of half the structure has been decomposed into  $2.068 \times 10^6$  8-nodes hexahedral volume elements, for  $10.34 \times 10^6$  degrees of freedom (DOF) on the whole (5 DOF for each volume element: the 3 displacement components and the pressure of the volume element centroid plus the EVF, [ABAQUS, 2016]).

In Coupled-Eulerian-Lagrangian (CEL) simulations, ABAQUS/Explicit takes into account for the Eulerian fluid domain through the so-called volume-of-fluid method: the material flowing through the mesh is tracked by the definition of an additional variable within each element, the Eulerian volume fraction (EVF). In our case, this allows to compute not only the propagation of the shock waves, but also the diffusion of the explosive material inside the air domain. The coupling between the Lagrangian (solid) domain and the Eulerian (fluid) one, i.e. the fluid-structure interaction, is achieved by a general contact algorithm, with a null interface friction coefficient and a penalty method.

Boundary conditions on the Eulerian domain are of two kind: a reflecting boundary is used for the symmetrical plane, while a nonreflecting outflow condition is applied to the other surfaces. The first one imposes a zero flow across the boundary, i.e. zero normal velocities. The nonreflecting outflow condition consists, instead, of the application of additional normal and shear tractions on the domain boundary that are proportional to normal and shear components of the velocity at the boundary. In a sense, it consists on using damping constants in order to minimize the reflection of waves back into the fluid domain. However, the need for achieving a condition similar to plane body waves impinging on the boundary surfaces requires to extend the Eulerian domain beyond the solid domain. This is why we have modeled a volume of air as deep as 5 meters above the *oculus* and a volume of 2 meters of air on the lateral sides.

The choice of the fineness of the mesh has been done upon a convergence analysis: four different meshes for the air domain have been considered: M1, with  $1.48 \times 10^6$  DOF, M2 with  $6.3 \times 10^6$  DOF, M3, the chosen mesh detailed above, and a reference mesh M4, the finest one, with  $16.94 \times 10^6$  DOF.

For each mesh, we have computed the blast overpressure in correspondence of three different observation points: P1, P2 and P3, indicated in Fig. 9, respectively close to the base of the cylindrical wall, to its top and to the *oculus*. The time histories of the overpressure, for the three different points and for each mesh, are plotted in Fig. 10 (the curves has been normalized with respect to the highest value).

In Fig. 11 we show, for points P1 to P3, the relative error evaluated for meshes M1 to M3 with respect to mesh M4; such an error, in percent, is computed as

$$err = 100 \left| \frac{p_{Mi} - p_{M4}}{p_{M4}} \right|, \quad (16)$$

where  $p_{Mi}$  is the peak of the overpressure, in P1, p2 or P3, evaluated for mesh  $M_i$ , while  $p_{M4}$  is the same for the reference mesh M4.

Considering the results shown in Fig. 10 and 11, we can see that the choice of the mesh M3 is a fair compromise: it guarantees a good quality of the result (the maximum relative error is 3.8%, for point P3) with a problem size that is not extreme.

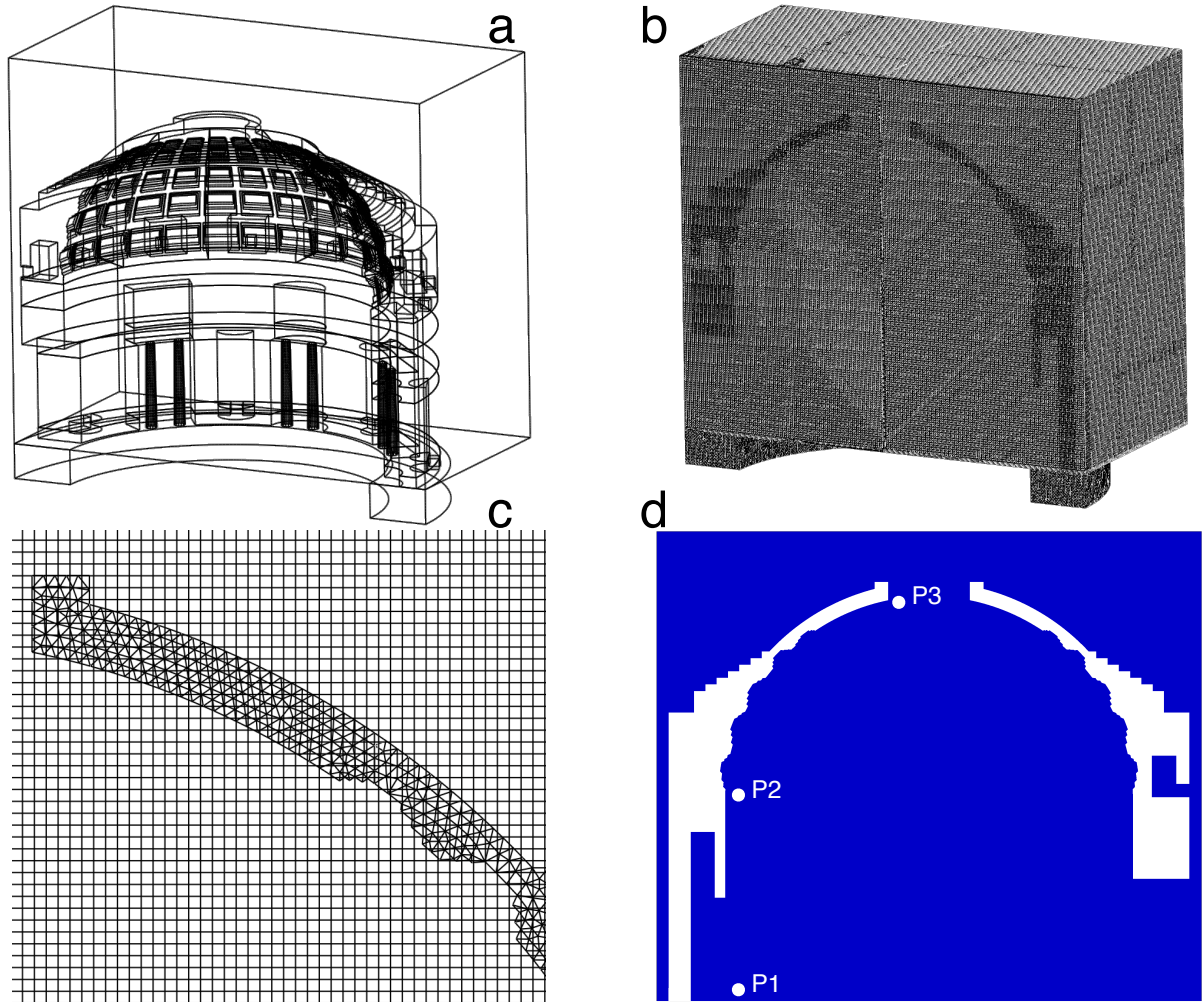


Figure 9: The air domain; a) overall view, b) complete mesh, c) detail of the mesh, c) location of the observation points P1 to P3.

We have also compared the results given by JWL with those given by CONWEP for the reflected pressure  $P_r$  on the solid points corresponding to P1, P2 and P3, see Fig. 12 (the curves have been normalized with respect to the highest value). The comparison clearly shows how much the use of CONWEP in a case like this one can lead to erroneous results: the time history of the overpressure is completely different, mainly due to the reflected shock waves.

## 5.2 Validation of the Pantheon finite elements model

The entire structure of the Pantheon has been modeled using the CAD programs, see Fig. 13. The model comprehends the coffering of the dome intrados, the step-rings, the interior columns, absides and cavities present in the cylindrical wall and the foundation ring.

The CAD model has been successively meshed to obtain a finite element (FE) model. The FE model comprehends only the *Rotonda*, because the structural role of the *pronaos*

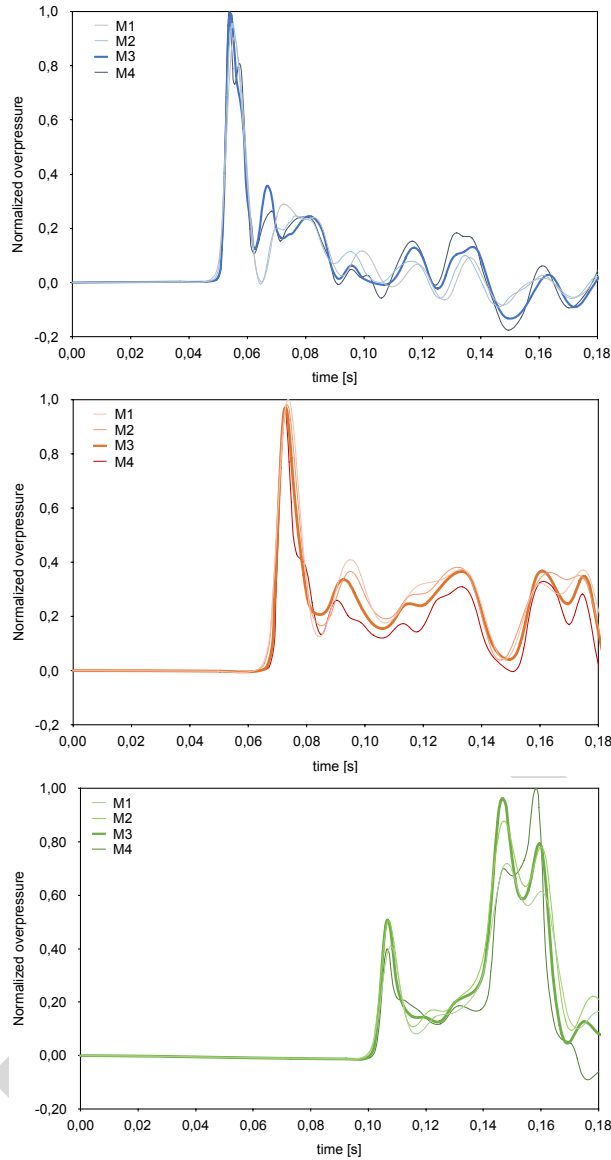


Figure 10: Time history of the overpressure for points P1 to P3 (from the top).

is undoubtedly little, for the blast actions of an explosion in the interior of the Pantheon; so, we have neglected it.

Just like for the mesh of the air domain, we have performed a convergence analysis for validating the choice of the *Rotonda* mesh, composed of four-nodes tetrahedral elements, supported by both the standard and explicit solvers of ABAQUS.

Also in this case, the fineness of the mesh has been chosen after a convergence analysis, performed in order to obtain a reliable degree of accuracy with an acceptable size of the whole numerical model (air domain plus structure).

The convergence analysis has been done using the standard (implicit) scheme for eleven different structural meshes  $MS_i$ ,  $i=1, \dots, 11$ , whose characteristics are given in Tab. 4.

The standard analysis made for each mesh  $MS_i$  is divided into two parts: a modal analysis and a static one, for the only gravity load. We have monitored the eigenfrequencies of

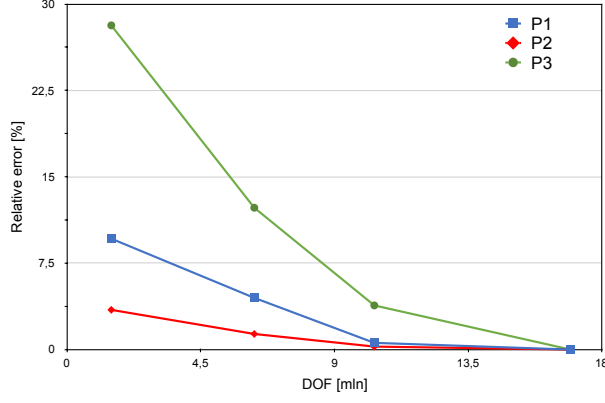


Figure 11: Relative error, eq. (16), for points P1 to P3 as function of the number of DOF.

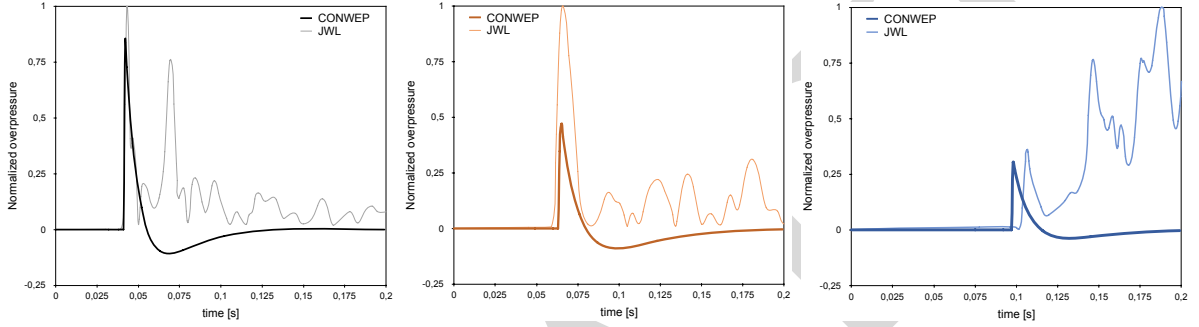


Figure 12: Comparisons of  $P_r$  time history as evaluated by JWL and CONWEP; from the left, comparison for points P1, P2, P3.

the first twenty vibration modes of the structure and, for the static analysis, the vertical displacement of point P3 in Fig. 10. The twenty eigenfrequencies  $f_j$ ,  $j = 1, 2, \dots, 20$ , and the vertical displacement  $u$  of the point P3, are calculated for each structural mesh MS. The convergence has been evaluated like for the air domain, calculating for each mesh MS $_i=1, \dots, 10$  the errors  $\Delta f_j$  of the frequencies  $f_j$  and  $\Delta u$  of the displacement  $u$ , relatively to the same quantities  $f_j^r$  and  $u^r$ , calculated for the reference mesh MS11, the finest one:

$$\Delta f_j = \left| \frac{f_j - f_j^r}{f_j^r} \right|, \quad j = 1, 2, \dots, 20, \quad \Delta u = \left| \frac{u - u^r}{u^r} \right|, \quad \forall \text{MS} = 1, \dots, 10. \quad (17)$$

In Fig. 14 we show the diagrams of  $\Delta f_1$ ,  $\Delta f_{10}$  and  $\Delta f_{20}$  along with  $\Delta u$  as functions of the DOF number.

In Fig. 15 left we report the cumulative normalized CPU time necessary for the static and modal analysis as function of the DOF number; for each mesh MS $_i$ ,  $i=1, \dots, 11$ , this is the ratio between the CPU time corresponding to MS $_i$  and that of MS1. In Fig. 15 right, we show the relative errors  $\Delta f_1$ ,  $\Delta f_{10}$ ,  $\Delta f_{20}$  and  $\Delta u$  versus the normalized CPU time.

After evaluation of the results in Fig. 14 and 15, we have selected the mesh MS11, the finest one, for the computations. In fact, we have estimated that the convergence has been reached (the diagrams in Fig. 14 and 15 show an asymptotic behavior) while the increase

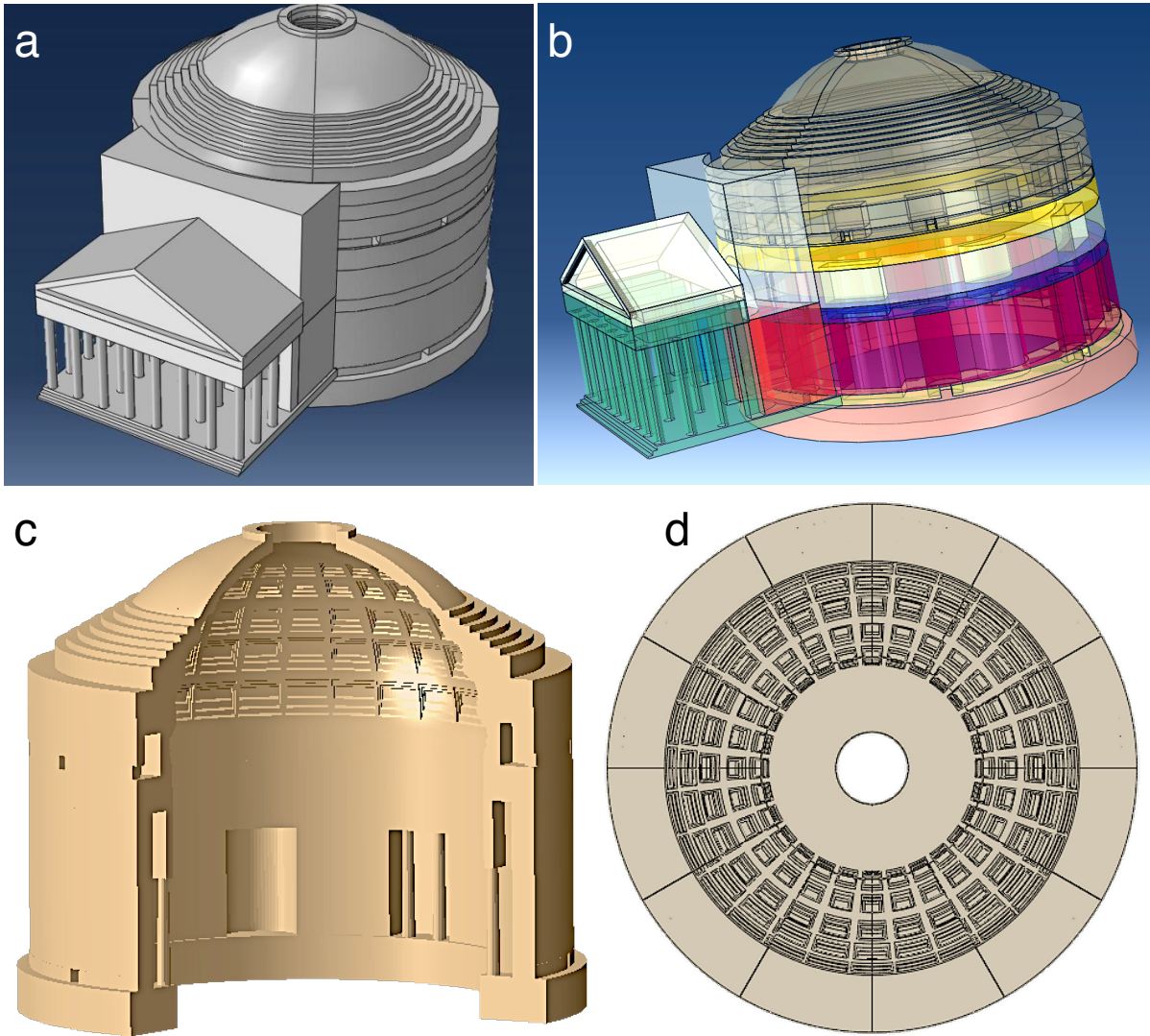


Figure 13: The CAD model of the Pantheon; a): overall view, b) transparency view, c) interior view of the *Rotonda*, d) detail of the dome with indicated the twelve meridional cracks inserted in the model.

of the computation time can still be considered as tolerable. A detail of the structural mesh MS11 is shown in Fig. 16.

To take into account for the existing cracks in the dome, Fig. 3, we have modeled 12 cracks, propagating along the meridians up to  $57^\circ$  above the plane passing through the sphere center in Fig. 2 and equally spaced; they are indicated in Fig. 13 d).

Parallel computing is used to decrease significantly the length of the analyses. All the simulations have been performed using a 24-cores workstation. The entire model is, thus, divided into 24 geometric domains, taking advantage of the 24 processors of the machine.

Table 4: Characteristics of the studied structural meshes.

Mesh	Average element size [m]	Number of elements	Number of DOF
MS1	1.80	95000	74000
MS2	1.60	122200	94000
MS3	1.40	159300	118000
MS4	1.20	224000	160000
MS5	1.00	348000	240000
MS6	0.80	590000	390000
MS7	0.60	1200000	750000
MS8	0.55	1500000	960000
MS9	0.50	1980000	1200000
MS10	0.45	3450000	2060000
MS11	0.35	4800000	2800000

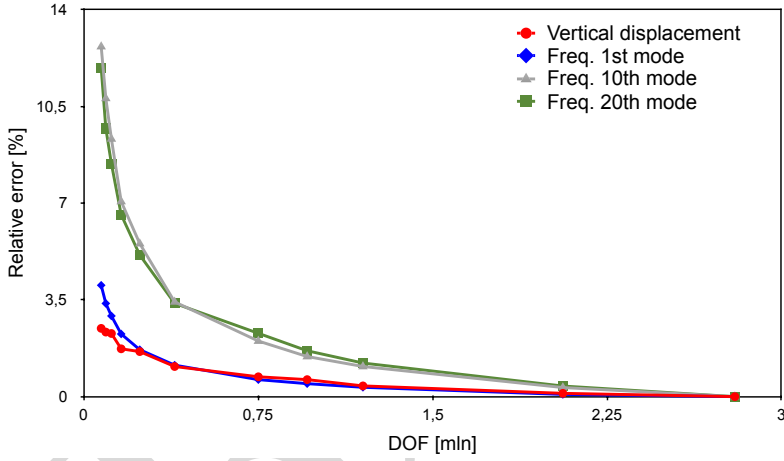


Figure 14: Relative errors  $\Delta f_1$ ,  $\Delta f_{10}$ ,  $\Delta f_{20}$  and  $\Delta u$  as function of the number of DOF.

## 6 Numerical simulations

We have simulated the effects of an explosion in the center of the *Rotonda*; some images representing the simulation at different times are represented in Figs. 17 to 21. The pictures represent the pressure field in the interior of the *Rotonda* and, starting from the moment where the first cracks appear in the dome, the effects on the structure, where the propagation of cracks is clearly visible. We comment separately the pressure field and the effects on the structure.

### 6.1 Evolution of the pressure field

The pressure field represented in Figs. 17 to 20 is comprehensive of all the blast phenomena: shock wave, reflected shock waves and dynamic pressure. The first two sketches in Fig. 17 show the very initial phases of the blast, with the shock wave propagating

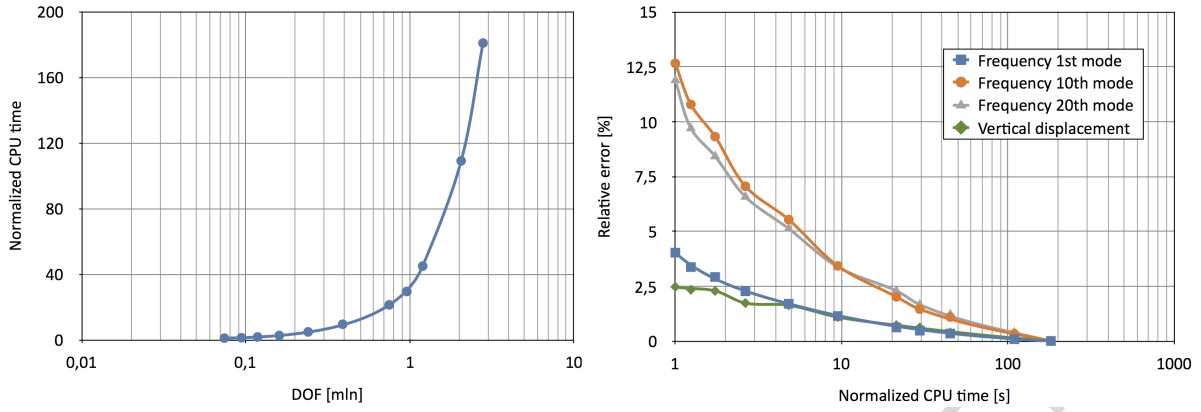


Figure 15: Normalized CPU time as function of the DOF number, left, and relative error versus the normalized CPU time, right.

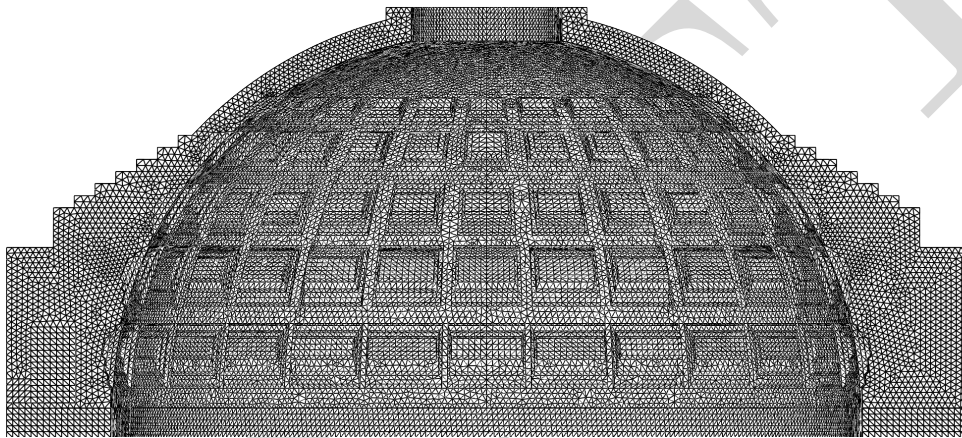


Figure 16: Detail of the structural mesh MS11.

hemispherically until it touches the cylindrical wall. At this moment, the reflected shock waves add to the principal one, creating a complex pressure field and, though the principal shock wave decreases in intensity, important local concentrations of pressure are possible due to the interaction between the principal shock wave and the reflected ones.

Local concentration of the pressure are clearly visible in the interior of the niches and in the parts of the coffering looking downward, but the most important concentration happens exactly in the central axis of the *Rotonda*, of course as an effect of its cylindrical symmetry. An important zone of high pressure, in the form of a butterfly, forms and progresses towards the *oculus*. This last represents an important escape way for the pressure and the gases, as clearly visible in the pictures of Fig. 18. Also the entrance door is an escape way, but apparently it has a least effect of the *oculus*, because the focalized shock waves move toward the dome's top.

Such pressure concentrations can lead to local value of the overpressure far greater than that produced by the original shock wave. This is clearly visible, e.g., in Fig. 10, where the pressure for point P3, close to the *oculus*, clearly shows secondary peaks far higher than the first one, due to the impinging shock wave. These secondary peaks mark the passage, through the *oculus*, of the "butterfly" pressure wave. Another important fact, still visible in Fig. 10, is the fact that the overpressure lasts much more than the single

original shock wave. Of course, this has a strong effect on the damage of the structure, because it is much longer exposed to high impact pressures.

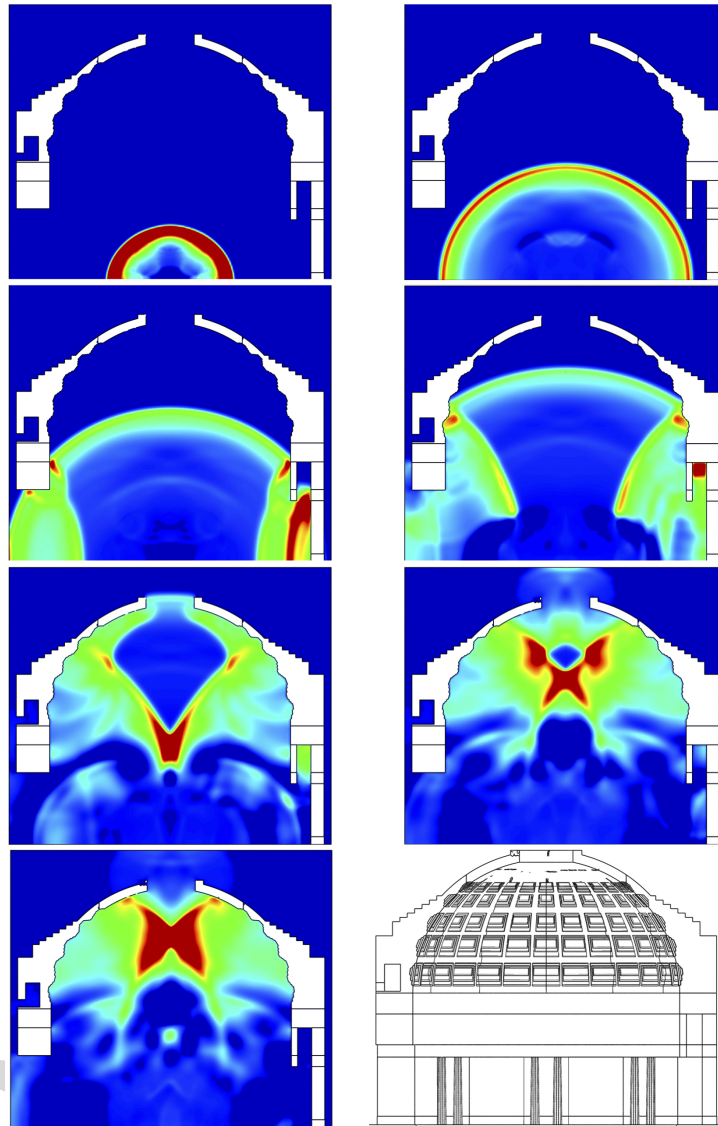


Figure 17: The simulation of a blast inside the *Rotonda*.

Rather surprising is the fact that the coffers acts like dampers of the pressure impulse, in terms of both its module and time. On one hand, the sharp-cornered surfaces of the coffers are nothing but obstacles to the propagation of the internal blast wave: the waves reflected by the coffering array looking downward contrast the rising incident wave through the particular combination of incident and reflection angles, as clearly shown in Fig. 17. The arrangement of the coffers themselves results in a step-by-step attenuation, mitigating the incident pressure as getting closer to the upper part of the dome and the intense, butterfly-shaped, concentration that rises in the center of the *Rotonda*. On the other hand, this translates in a temporal phasing of the blast wave, well visible in Fig. 12. Indeed, comparing the pressure time history of the empirical model CONWEP with that from JWJ, one can see that the pressure impulse from the latter one arrives at the *oculus*, i.e. at point P3, delayed with respect to that computed by CONWEP. Therefore,

we can assess that the role of the coffering is structurally crucial: it serves not only to reduce the dome's weight but it is able also to mitigate the effects of an internal blast.

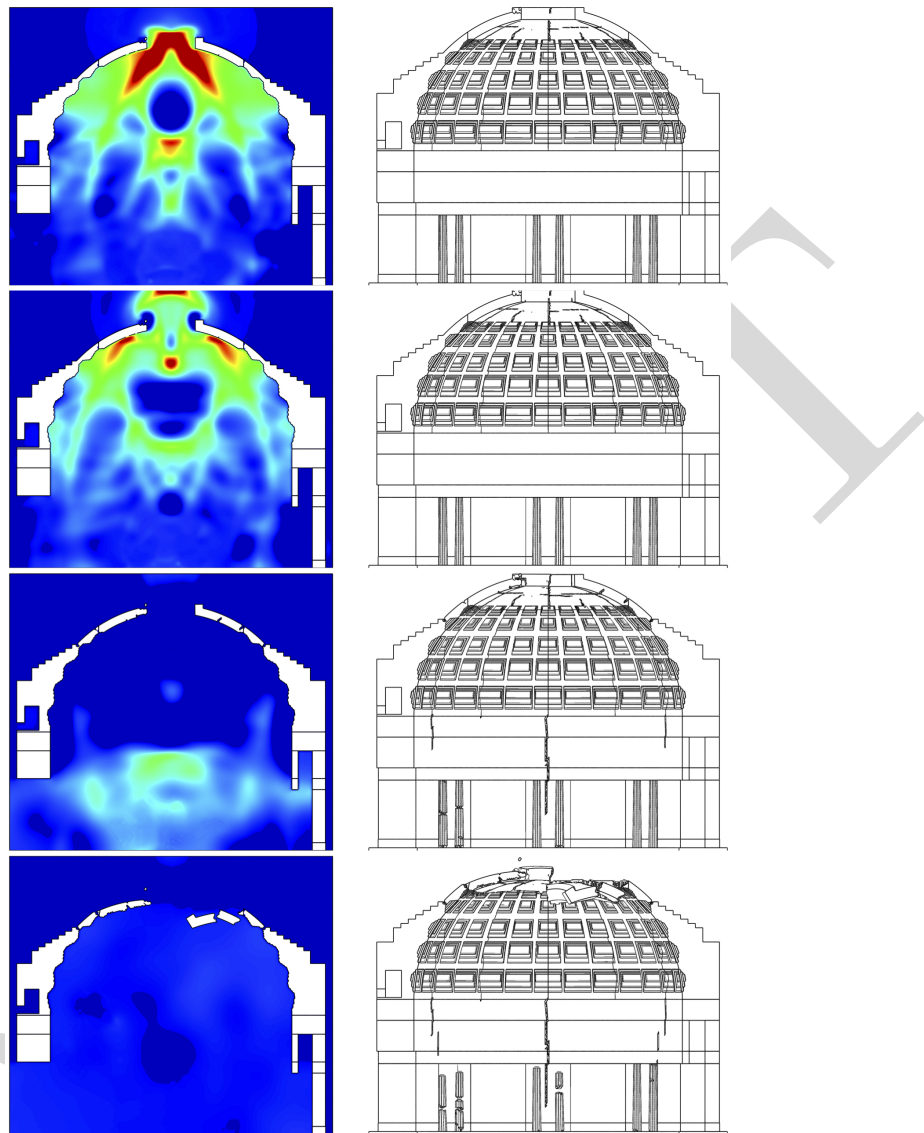


Figure 18: The simulation of a blast inside the *Rotonda* (continued).

## 6.2 Evolution of the structural damage

It is exactly the "butterfly" zone of focalized pressure, result of the interaction of the principal and reflected shock waves, that produces the principal damages to the *Rotonda*, and in particular it is likely to cause the destruction of the dome.

This is apparent looking at Figs. 19 and 20: the first cracks appear in the compression ring of the *oculus* when the focalized pressure approaches the dome and when it passes through the *oculus*, the existing cracks begin to propagate toward the dome's top and eventually they reach it. The static regime of the dome is completely changed, because

a shell behavior is no more possible and, each part of the dome behaving like a wedged cantilever, a circular crack appears in the upper part of the dome as consequence of the bending tensile stresses produced by gravity so that, in the end, the upper part of the dome falls down to ground.

In the same time, the lower part of the *Rotonda*, the cylindrical wall, is interested by cracks, that propagate through the entire wall thickness starting from the existing ones, as apparent in Figs. 20 and 21, while also the granite columns are fractured by the blast.

The failure of the dome is hence the consequence of different causes: the blast, the propagation of the existing cracks and the weight of the dome itself.

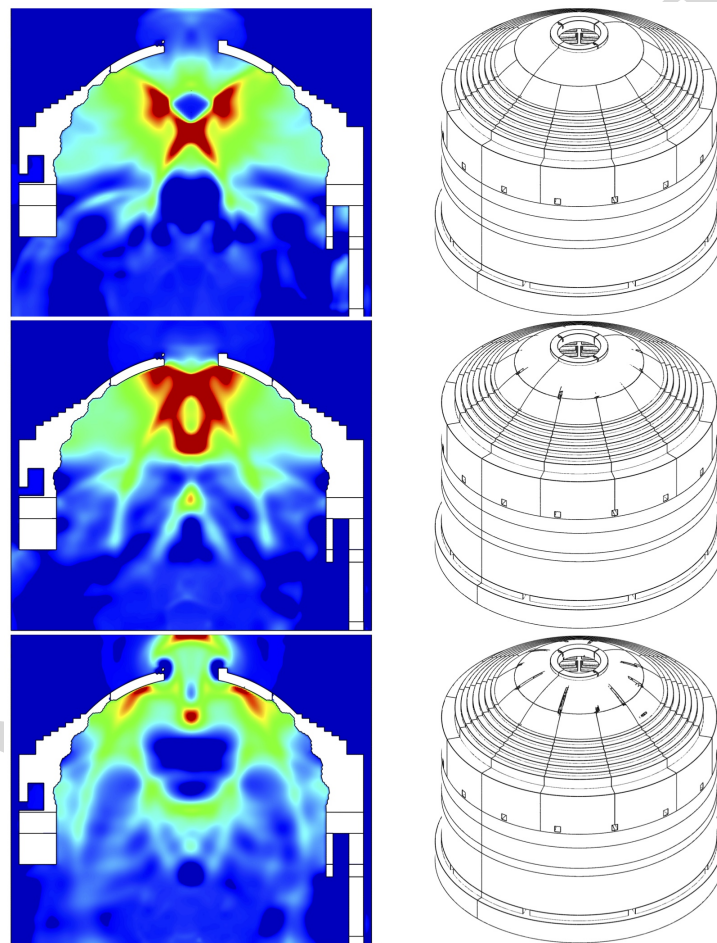


Figure 19: The simulation of a blast inside the *Rotonda*; external view.

The real extent of the existing cracks in the *Rotonda's* dome is uncertain. So, for the sake of completeness, we have performed the same simulation described above and on exactly the same model of the Pantheon but now without the existing cracks. All the other parameters are left unchanged.

The results of this analysis are shown in Fig. 22, where the two cases of structure with or without cracks are compared at different instants. Looking at these pictures, it is evident that the case without cracks has a different failure mechanism: the upper part of the dome is still destroyed, but to a less extent with respect to the case with cracks.

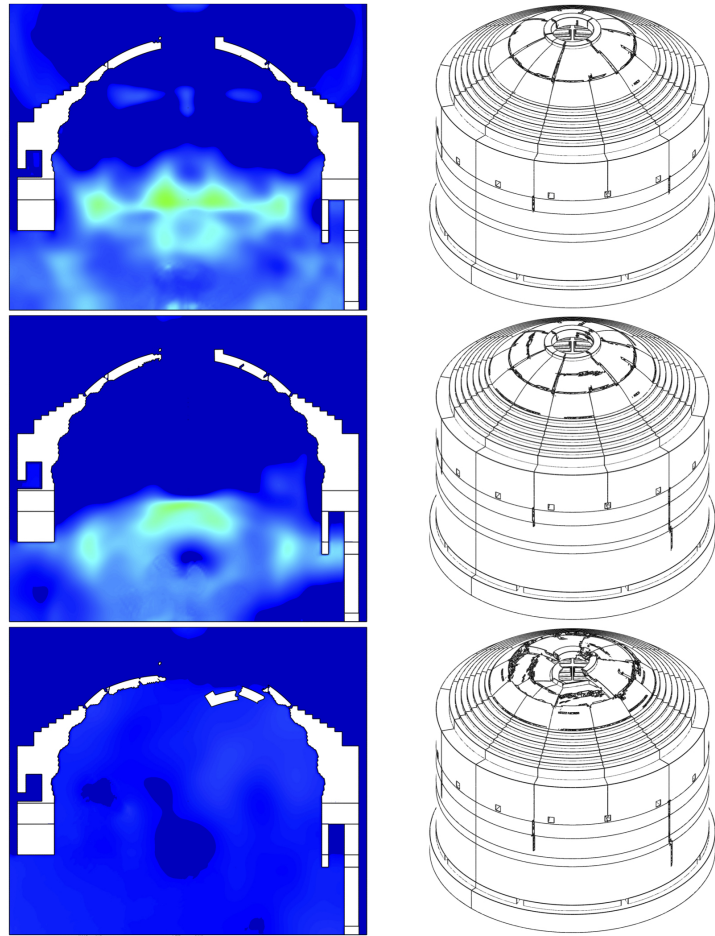


Figure 20: The simulation of a blast inside the *Rotonda*; external view (continued).

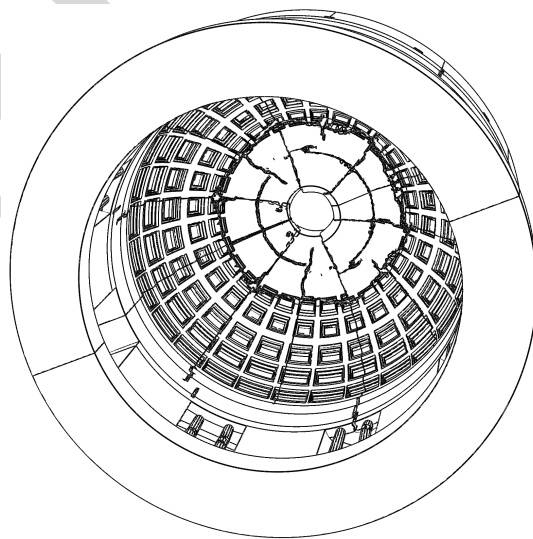


Figure 21: The simulation of a blast inside the *Rotonda*; internal view of the final situation.

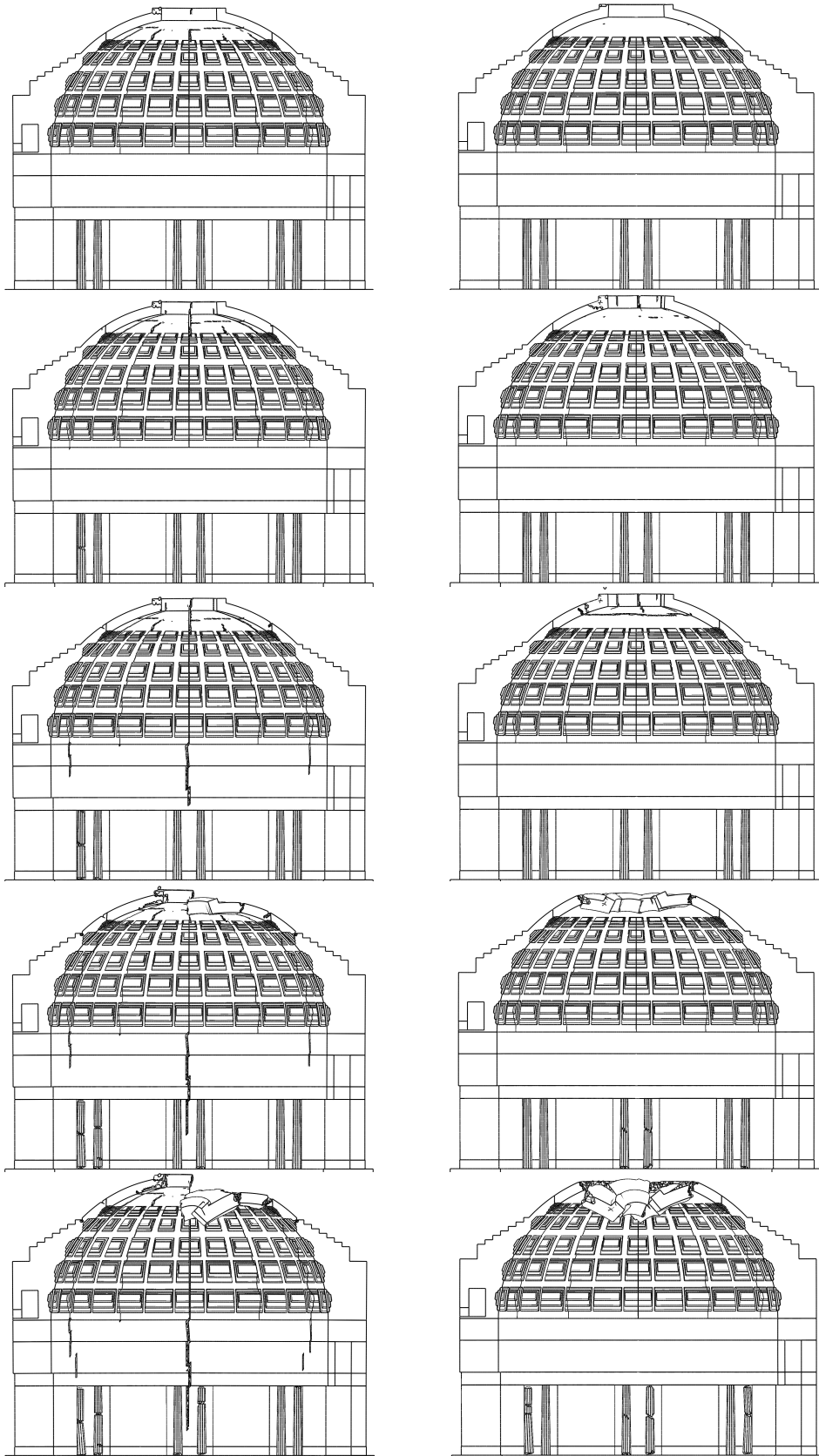


Figure 22: Comparison between the case with existing cracks (on the left) and without cracks (on the right).

This is because in the case of the cracks, as mentioned above, the blast effect is a propagation of these toward the top of the dome and the creation of the cantilever effect, that destroy a large part of the dome under the action of the gravity. In the case without cracks, the upper part of the dome is destroyed mainly by the cracks produced at the intrados by the blown of the blast. Moreover, while in the case with cracks these propagates also downward in the cylindrical wall of the *Rotonda*, this last is practically unaffected by the explosion, apart the granite columns. As a conclusion, we can say that also if the existing cracks are ignored in the simulation, the dome is destroyed by the blast, though to a less extent, while the cylindrical wall remains almost intact. The existing cracks constitute hence a weakness of the whole structure of the Pantheon for what concerns the effects of an explosion.

### 6.3 Considerations about the numerical simulations

The results presented hereon have been produced by a numerical simulation; though there is always, in such a kind of problems, a certain ineradicable difference between reality and simulation, nevertheless they certainly grasp the main response of the structure to a blast.

For what concerns the simulation of the blast itself, it clearly shows how much it is important to take into account for reflected shock waves, a fundamental aspect of the phenomenon for internal explosions. This means that a study of such phenomena done using empirical models like CONWEP, not taking into account for reflected shock waves, can lead to results really far from reality and principally underestimate the effects of the blast on the structure.

The response of the structure deserves a commentary. The results shown hereon have been obtained for the least quantity of explosive able to destroy, at least in part, the Pantheon. Without entering in details, we precise that such a quantity is really enormous, impossible to be brought in the interior of the *Rotonda* by hands, without some mechanical means.

In other words, the Pantheon is intrinsically safe with respect to explosions. This is due to different reasons. On one hand, its dimensions: it is a large building and the structure itself is really massive: the cylindrical wall thickness is  $\sim 6$  m, while that of the dome of  $\sim 1.5$  m at its top, as already mentioned. Then, its form: the cylindrical form is by itself more likely to resist to impact pressures than a flat one, more exposed to bending stresses. Finally, and this point is really surprising, the material. As already highlighted in Sec. 4.2, Roman concrete has mechanical properties quite different from modern light concretes: its Young's modulus ( $\sim 3$  to  $\sim 18$  GPa, [Brune, 2010], [Lamprecht, 1984]), good tensile strength,  $\sim 0.6$  MPa, and fracture energy,  $\sim 60$  J/m<sup>2</sup>, confer to Roman concrete very good properties of resilience and shock absorbing. Though, of course, ancient Romans did not conceive this material for absorbing a blast effects, nevertheless it reveals once more to be a key of the structural success of the Pantheon.

## Acknowledgments

We wish to thank D. Gomes and I. Naciri, two students of Master DSME of University of Versailles, who realized the CAD model of the Pantheon.

We are pleased to thank Dr. Arch. E. Pulvirenti for her kindness in allowing us to publish her pictures of the Pantheon.

## References

- ABAQUS. Abaqus analysis user's guide. Technical Report Abaqus 6.14 Documentation, Simulia Corp., 2016.
- ACI. Guide for structural lightweight aggregate concrete. Technical report, American Concrete Institute, 1999.
- C. B. Boyer. *A history of mathematics*. J. Wiley & Sons, New York, 1968.
- Ph. F. Brune. *The Mechanics of Imperial Roman Concrete and the Structural Design of Vaulted Monuments*. PhD thesis, Department of Mechanical Engineering - University of Rochester, Rochester, NY, 2010.
- Ph. F. Brune, R. Perucchio, A. R. Ingraffea, and M. D. Jackson. The touchness of imperial roman concrete. In B. H. Oh et al., editor, *Recent advances in fracture mechanics of concrete*, pages 38–45, Seoul, South Korea, 2010. Korea Concrete Institute.
- O. Buyukozturk. Interface fracture and crack propagation in concrete composites. In C. Huet, editor, *Micromechanics of concrete and cementitious composites*, pages 203–212, Lausanne, Switzerland, 1993. Presses Polytechniques et Universitaires Romandes.
- M. Como. *Statics of historic masonry constructions*. Springer Verlag, Berlin, Germany, 2013.
- F. Dehn. Fracture mechanical behaviour of lightweight aggregate concrete. In *Fracture mechanics of concrete structures. Proceedings of International conference on fracture mechanics of concrete and concrete structures.*, Vail, Colorado, 2004.
- H. Draganic and V. Sigmund. Blast loading on structures. *Technical Gazette (Croatia)*, 19:643–652, 2012.
- FIB. Lightweight aggregate concrete. Technical report, International Federation for Structural Concrete, 2000.
- J. Heyman. *The stone skeleton*. Cambridge University Press, Cambridge, UK, 1995.
- A. Hillerborg. Results of three comparative test series for determining the fracture energy  $G_f$  of concrete. *Matériaux et Constructions*, 18:407–413, 1985.
- A. Hillerborg, M. Mod er, and P. E. Petersson. Analysis of crack formation and crack growth in concrete by means of fracture mechanics and finite elements. *Cement and Concrete Resistance*, 6:773–782, 1976.

- M. D. Jackson, J. M. Logan, B. E. Scheetz, D. M. Deocampo, C. G. Cawood, F. Marra, M. Vitti, and L. Ungaro. Assessment of material characteristics of ancient concretes, Grande Aula, Markets of Trajan, Rome. *Journal of Archaeological Science*, 36:2481–2492, 2009.
- M. D. Jackson, Eric N. Landis, Ph. F. Brune, M. Vitti, H. Chen, Q. Li, M. Kunz, H.-R. Wenk, P. J. M. Monteiro, and A. R. Ingraffea. Mechanical resilience and cementitious processes in Imperial Roman architectural mortar. *PNAS*, 111:18484–18489, 2014.
- H. Jones and A. R. Miller. The detonation of solid explosives. *Proc. Royal Soc. A*, 194:480, 1948.
- K. de Fine Licht. *The Rotunda in Rome: a study of Hadrian's Pantheon*. Jutland Archeological Society, Copenhagen, Denmark, 1968.
- V. Karlos and G. Solomos. Calculation of Blast Loads for Application to Structural Components. Technical report, Joint Research Center of the European Commission, 2013.
- C. N. Kingery and G. Bulmash. Technical report ARBRL-TR-02555: Air blast parameters from TNT spherical air burst and hemispherical burst. Technical report, U.S. Army Ballistic Research Laboratory, 1984.
- Z. Koccaz, F. Sutcu, and N. Torunbalci. Architectural and structural design for blast resistant structures. In *Proc. of 14th World Conference on Earthquake Engineering*, Beijing, 2008.
- H. O. Lamprecht. *Opus caementicium: Bautechnik der Römer*. Beton-Verlag, Düsseldorf, Germany, 1984.
- L. C. Lancaster. *Concrete Vaulted Construction in Imperial Rome*. Cambridge University Press, New York, NY, 2005.
- E.L. Lee, H.C. Horning, and J.W. Kury. Adiabatic expansion of high explosives detonation products. Technical Report TID 4500 - UCRL 50422, Lawrence Livermore National Laboratory, 1968.
- R. Mark. *Light, wind and structure*. The MIT Press, Cambridge, Massachusetts, 1990.
- R. Mark and P. Hutchinson. On the Structure of the Roman Pantheon. *The Art Bulletin*, 68:24–34, 1986.
- T. Ngo, P. Mendis, A. Gupta, and J. Ramsay. Blast loading and blast effects on structures - An overview. *Electronic Journal of Structural Engineering*, Special Issue: Loading on Structures:76–91, 2007.
- R. Perucchio and Ph. F. Brune. Concrete vaulting in Imperial Rome: A structural analysis of the Great Hall of Trajan's Markets. In J. F. Abel and J. R. Cooke, editors, *Proc. of the 6th International conference on Computation of Shell and Spatial Structures*, Cornell University, Ithaca, NY, 2008.
- R. Perucchio and Ph. F. Brune. The Evolution of Structural Design of Monumental Vaulting in Opus Caementicium in Imperial Rome. In *Proceedings of the Third International Congress on Construction History*, Cottbus, Germany, May 2009.

- E. Pulvirenti. Didatticarte, 2014. URL <http://www.didatticarte.it/Blog/?p=2169>.
- A. M. Remennikov. A review of methods for predicting bomb effects on buildings. *J of Battlefield Techn*, 6:5–10, 2003.
- A. Samuelli-Ferretti. Materiali da costruzione e tecnologie costruttive del patrimonio archeologico e monumentale romano con particolare riferimento al tipo laziale ed all’opus latericium. Technical report, Dipartimento di Ingegneria Strutturale e Geotecnica - University of Rome "La Sapienza", Rome, Italy, 1996.
- L. Sanpaolesi and P. Formichi. *Calcestruzzo leggero strutturale di argilla espansa*. Leca, Parme, Italy, 2009.
- I. Stefanou, K. Sab, and J.-V. Heck. Three dimensional homogenization of masonry structures with building blocks of finite strength: A closed form strength domain. *International Journal of Solids and Structures*, 54:258–270, 2015.
- A. Terenzio. La restauration du Panthéon de Rome. In *La Conservation des Monuments d’Art & d’Histoire*, pages 280–285. Office International des Musées, Paris, France, 1934.
- USACE. TM 5-855-1: Design and Analysis of Hardened Structures to Conventional Weapons Effects. Technical report, U. S. Army, 1986.
- USACE. TM 5-1300: Structures to Resist the Effects of Accidental Explosions. Technical report, U.S. Army, 1990.
- USACE. UFC 3-340-02: Structures to Resist the Effects of Accidental Explosions. Technical report, U.S. Army, 2008.
- P. Vannucci, F. Masi, and I. Stefanou. A study on the simulation of blast actions on a monumental structure. *International Journal of Mechanical Sciences*, (submitted), 2017a. URL <https://hal.archives-ouvertes.fr/hal-01447783v3/document>.
- P. Vannucci, I. Stefanou, and F. Masi. Report of the project "Cathédrales durables". Technical report, CNRS, Paris, France, 2017b.
- J. Weerheijm and I. Vejt. The dynamic fracture energy of concrete. Review of test methods and data comparison. In B. H. Oh et al., editor, *Recent advances in fracture mechanics of concrete*, pages 419–427, Seoul, South Korea, 2010. Korea Concrete Institute.
- M. L. Wilkins. The equation of state of PBX 9404 and LX 04-01. Technical Report UCRL - 7797, Lawrence Radiation Laboratory, 1964.
- M. Wilson-Jones. *Principles of Roman Architecture*. Yale University Press, New Haven, Connecticut, 2000.